

# Multipath Exploitation-Based Linearized Inverse Scattering Method for Non-Line-of-Sight Indoor Imaging of PEC Objects

Hiroshi Suenobu <sup>1</sup>, Member, IEEE, Shouhei Kidera <sup>2</sup>, Senior Member, IEEE, Takayuki Nakanishi, Member, IEEE, Ryosuke Kobayashi, Yasuhiro Nishioka, Member, IEEE, and Yoshio Inasawa, Senior Member, IEEE

**Abstract**—This article reports on the localization and imaging of perfect electric conductive (PEC) objects in a non-line-of-sight (NLOS) environment using the multipath exploitation-based inverse scattering method. We considered the application of the linearized inverse scattering method, using the physical optics approximation for the scattering analysis from a metallic object to imaging scatterers located in the NLOS area. By assuming that the geometry of the NLOS environment is known, we can obtain the numerical Green's function, which includes multipath propagation components between the observation points and the imaging region, and connect them within the geometry. This enables the inverse scattering method to be applied to NLOS targets. As a typical NLOS scenario, we assumed an indoor T-junction scenario for collision avoidance and adopted the formulation of the method as two-dimensional planar imaging to the scenario and validated its imaging performance in the NLOS area through the three-dimensional electromagnetic simulations and experiments in an anechoic chamber using a 2 GHz band radar system. These validations demonstrated that our proposed scheme can accurately reconstruct a metallic plate-shaped object in the NLOS area.

**Index Terms**—Inverse scattering, multipath exploitation, non-line-of-sight (NLOS), radar imaging.

## I. INTRODUCTION

IN recent years, short-range radar sensing technology has been expanded to numerous sensing applications such as for autonomous driving, autonomous mobile robots (AMR), advanced driver-assistance systems, and for detecting concealed items in security screening. Especially, to overcome the traditional limitations of radar sensing, the imaging or identification of objects in non-line-of-sight (NLOS) areas is being highlighted as an emergent application.

In microwave or millimeter wave propagation, significant echoes from objects in the NLOS area occur due to the diffraction

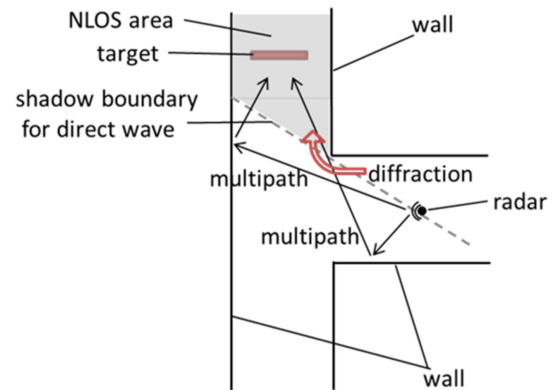


Fig. 1. Example of the typical NLOS environment.

effect at the edges of obstructions, or multiple reflections between the target object and surrounding surfaces. The abovementioned effect suggests that detecting, localizing, or identifying targets in the NLOS area is possible, and many studies focus on this effect [1], [2], [3], [4], [5], [6], [7], [8], [9], [10], [11], [12], [13], [14], [15], [16]. The study in [2] indicates that targets hidden behind obstructions can be detected and identified using diffraction signals produced by an obstacle's corners and edges. However, the intensity of the diffracted signal becomes much weaker than that of the direct waves, especially in the case of an object being completely occluded. Thus, because it is difficult to retain a sufficient signal-to-noise (S/N) ratio, such approaches can seldom be used when targets are located near the corner of an obstacle. Conversely, a typical indoor or urban NLOS geometry can be considered a T-junction (shown as Fig. 1) or an L-shape corner, and multipath components reflected between walls and objects possibly provide a higher S/N ratio compared to those of the waves diffracted by corners. However, since conventional radar imaging techniques do not consider multiple reflection paths, ghost images may arise due to multiple scattering components [3]. To address this, several researchers have developed methods that correctly localize or identify the position of the target hidden in an NLOS area [4], [5], [6], [7], e.g., identifying the path to the target using geometry information. Such processing schemes to improve the localization accuracy or the spatial resolution are termed multipath exploitation [8],

Received 29 August 2024; revised 2 November 2024 and 1 January 2025; accepted 21 January 2025. Date of publication 31 January 2025; date of current version 7 March 2025. (Corresponding author: Hiroshi Suenobu.)

Hiroshi Suenobu, Takayuki Nakanishi, Yasuhiro Nishioka, and Yoshio Inasawa are with the Mitsubishi Electric Corporation, Tokyo 100-8310, Japan (e-mail: Suenobu.Hiroshi@ab.MitsubishiElectric.co.jp).

Shouhei Kidera is with the Graduate School of Informatics and Engineering, The University of Electro-Communications, Tokyo 182-8585, Japan (e-mail: kidera@uec.ac.jp).

Ryosuke Kobayashi is with the Mitsubishi Electric Engineering Company Limited, Tokyo 102-0073, Japan.

Digital Object Identifier 10.1109/JSTARS.2025.3537181

[9]. Alternatively, there is also data driven based approach using machine learning reported in [10].

Furthermore, to focus on imaging the target's shape and position some approaches use synthetic aperture radar (SAR). Examples of applying SAR imaging to NLOS targets are reported in [11], [12], and [13]. The study in [12] discusses the suppression of ghost images caused by multipath components and imaging the shape of the obstructed target's hidden portion. For targets hidden by obstacles [14] reports a two-dimensional (2D) imaging method using waves reflected from a mirror in front of the open side of the radar and the targets (the obstacles are placed between the radar and the targets). Its three-dimensional (3D) imaging version is also reported in [15]. However, these methods basically require highly complex processing, such as identifying the paths of multipath components reaching the NLOS area, estimating equivalent observation points by assuming them to be direct waves, and estimating and correcting the phase error or rotation caused by reflections off objects with rough surfaces [16].

Several studies have proposed using linearized inverse scattering as an alternative low-complexity imaging approach [17], [18], [19]. By applying the physical optics approximation to the integral equation of the scattering problem, assuming an object with perfect electric conductivity (PEC), the inverse scattering problem is linearized, and the boundary distribution of the PEC object is obtained as the solution. Further applications of this approach are reported in [20], [21], [22], and [23]. In particular, Gennarelli and Soldovieri [22] applied this method to multipath-rich situations. The study uses a numerically obtained Green's function with known geometry for imaging the PEC object and enhances the resolution of images through the contributions of the multipath components. Furthermore, this implies the possibility of imaging an object in the NLOS area. By including the multipath effect of Green's function in advance, this approach avoids the complexity of the conventional method mentioned earlier. The through-the-wall radar imaging studies also report constructing a proper Green's function or a propagation model specialized to a specific scenario analytically or numerically [24], [25], [26], [27].

Our study focused on imaging a PEC target located in the NLOS area (hereafter termed the NLOS target) and imaging it by applying the linearized inverse scattering method based on the physical optics approximation proposed in [22] to a 3D T-junction geometry. This typical NLOS environment was used to examine the 2D imaging of NLOS targets as a PEC scattering problem. In general, not all target objects are made of PEC-like material. However, some typical targets can be assumed to consist of PECs in our targeting scenario, for example, autonomous moving robots (AMR) in the indoor environment, vehicles and bicycles in the outdoor environment, and the scattering characteristics of the human body behave approximately like PECs [28], [29]. We also focused on a formulation of 2D planar imaging of 3D objects to make it possible to work the method well. This limitation could be extended to 3D imaging by accumulating 2D slice images in further investigation [31]. The 3D geometry model was simulated and indoor experiments for the constructed T-junction geometry were performed in an anechoic chamber to verify the method's effectiveness.

The main contributions of this paper are following.

- 1) Applying the method suggested in [22] to the T-junction geometry as a typical NLOS situation.
- 2) Extending the method to a 3D problem and constructing a specific 2D planar imaging formulation that allows the method to work well in complex 3D geometry by introducing primal direction projection. It leads to applicability to different types of NLOS geometry without specialized signal modeling and algorithm modification to a specific geometry.
- 3) Verifying the 2D imaging of the PEC target in an NLOS area through a 3D electromagnetic simulation.
- 4) Performing indoor experiments in an anechoic chamber using a 2 GHz band radar system.
- 5) Confirming the method's efficacy through simulations and experiments.

The rest of this article is structured as follows: Section II describes the imaging method by the linearized inverse scattering method using the physical optics approximation, Section III describes how the linearized inverse scattering method was applied to the NLOS area, Section IV reports the verification by electromagnetic field simulation, Section V reports the experimental verification using an indoor geometry, and Section VI concludes the article.

## II. IMAGING BY INVERSE SCATTERING METHOD

This section discusses the imaging method that employs the linearized inverse scattering method using the physical optics approximation.

### A. Linearization By Physical Optics Approximation

The integral below (1) describes the relationship between the distribution of induced currents on the surface of a spatially distributed scatterer  $\mathbf{J}$  and the resulting scattered field  $\mathbf{E}^s$  [30]

$$\mathbf{E}^s(f, \mathbf{x}_O) = -j\omega\mu \int_S \mathbf{G}(f, \mathbf{x}_O, \mathbf{x}) \mathbf{J}(f, \mathbf{x}) dS. \quad (1)$$

Here,  $f$  is the frequency of the incident wave,  $\omega$  is the angular frequency,  $\mu$  is the permeability,  $\mathbf{G}$  is the dyadic Green's function in the tensor form, and  $S$  is the surface of the scatterer.  $\mathbf{x}_O$  represents the coordinates of the observation point, and  $\mathbf{x}$  represents the coordinates where the scatterer is located. To solve the distribution of the scatterer using the inverse scattering method, we use a distribution function  $s(\mathbf{x}) = \delta(\mathbf{x} - \mathbf{x}_S)$  to represent the unknown scatterer distribution and set the imaging region  $D$  [18]. Rewriting (1) by using  $s(\mathbf{x})$ , we have the following equation:

$$\mathbf{E}^s(f, \mathbf{x}_O) = -j\omega\mu \int_D \mathbf{G}(f, \mathbf{x}_O, \mathbf{x}) \mathbf{J}(f, \mathbf{x}) s(\mathbf{x}) d\mathbf{x}. \quad (2)$$

Here,  $d\mathbf{x}$  means  $dx dy dz$ ,  $s(\mathbf{x})$  is proportional to  $\delta(\mathbf{x} - \mathbf{x}_S)$ , where  $\mathbf{x}_S$  represents the coordinates where the scatterer surface exists, and  $\delta(\mathbf{x})$  is the Dirac delta function. It leads to a relationship  $\int_D \mathbf{J}(\mathbf{x}) s(\mathbf{x}) d\mathbf{x} = \int_S \mathbf{J}(\mathbf{x}) dS$ . The general conceptual illustration for the inverse scattering problem is shown in Fig. 2.

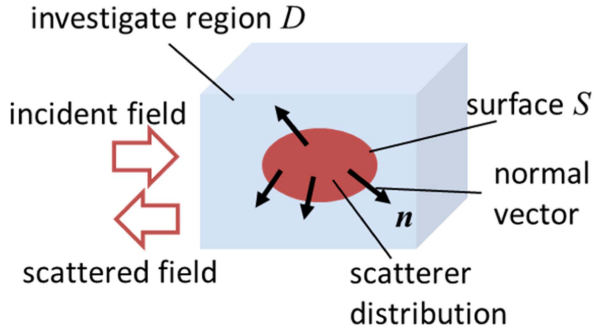


Fig. 2. Conceptual illustration for the inverse scattering problem.

The inverse scattering method aims to determine the distribution of scatterer  $s(\mathbf{x})$ , which induces the current distribution, from the measured scattered field  $\mathbf{E}^s$ . Since a current source at one position induces a current distribution at other positions, (1) is generally nonlinear. However, assuming that the scatterer has PEC and the current is localized on its surface, we can linearize it by applying the physical optics approximation with the incident magnetic field  $\mathbf{H}^{\text{inc}}$  and the normal vector field  $\mathbf{n}(\mathbf{x})$  associated with the distribution of the PEC object [18]. The current in this approximation acquires the following form:

$$\mathbf{J}(f, \mathbf{x}) \approx \mathbf{J}_{\text{PO}}(f, \mathbf{x}) = 2\mathbf{n}_s(\mathbf{x}) \times \mathbf{H}^{\text{inc}}(f, \mathbf{x}). \quad (3)$$

Here, if we define the normal vector field including the information of scatterer distribution as  $\mathbf{n}_s(\mathbf{x}) = \mathbf{n}(\mathbf{x})s(\mathbf{x})$ , it can be expressed as

$$\mathbf{n}_s(\mathbf{x}) = (n_x, n_y, n_z), \quad n_{x,y,z} \propto s(\mathbf{x}). \quad (4)$$

Then (2) becomes

$$\begin{aligned} \mathbf{E}^s(f, \mathbf{x}_O) = & -2j\omega\mu \int_D \mathbf{G}(f, \mathbf{x}_O, \mathbf{x}) \mathbf{n}_s(\mathbf{x}) \\ & \times \mathbf{H}^{\text{inc}}(f, \mathbf{x}) d\mathbf{x}. \end{aligned} \quad (5)$$

### B. Projection Procedure and Specific Formulation

Since the problem set up in a 3D environment is highly complex and the resulting linear system is highly ill-conditioned, the general formulation is difficult to work well directly. In this study, we introduce the following assumptions and approximations. First, we consider only 2D planar imaging of 3D objects and test only 2D imaging for vertically uniform objects. This restriction can be extended to 3D imaging by accumulating 2D slice images with vertical beam forming and the changing vertical position of the radar. Second, we approximate the normal vector distribution, an unknown to be solved in this formulation, as the direction vector mainly contributes to a scattered field. A component of the object surface facing the main path of energy transfer between the object and radar is mainly contributed to the measured scattered field. These assumptions can be expressed as

$$\begin{aligned} \mathbf{n}_s(\mathbf{x}) & \approx n^P(\mathbf{x}) \hat{\mathbf{p}}, \quad n^P(\mathbf{x}) = (\hat{\mathbf{p}} \cdot \mathbf{n}_s(\mathbf{x})) \\ \hat{\mathbf{p}} & = (\cos \phi^P, \sin \phi^P, 0). \end{aligned} \quad (6)$$

Here,  $\hat{\mathbf{p}}$  is a projection direction vector onto the supposed primarily direction of energy transmission on the imaging 2D plane (the  $x$ - $y$  plane) and  $\phi^P$  is the angle of the projection direction vector measured from the  $x$ -axis,  $n^P(\mathbf{x})$  is projected components of the normal vector distribution. We call this procedure primal direction projection. In this study, we deal with the T-junction geometry. In that environment, the main direction of the path of energy transfer  $\phi^P$  can be thought of as the direction NLOS imaging area to the center of the T-junction. If the actual object surface normal is vertical to the assumed direction  $\phi^P$ , this imaging method would not work, but such an object can be considered difficult to image or detect even in other approaches because it does not have a sufficient cross section to produce a scattered field observed by the radar. On the other hand, for example, if the actual object surface normally deviated  $45^\circ$  from the projected direction  $\phi^P$ , even in deviation of the imaging plane, the method held 70% of the source contribution producing scattered field by the object. There is sufficient possibility to capture the shape of the true boundary of the object. Thus, we only try to solve the component of normal vectors projected in the main direction, denoted as  $n^P(\mathbf{x})$ . Additionally, we consider a specific polarized component of the scattered field denoted as  $E_s$ . Therefore, (5) becomes

$$\begin{aligned} E^s(f, \mathbf{x}_O) = & -2j\omega\mu \int_D \bar{\mathbf{G}}(f, \mathbf{x}_O, \mathbf{x}) \\ & \hat{\mathbf{p}} \times \mathbf{H}^{\text{inc}}(f, \mathbf{x}) n^P(\mathbf{x}) d\mathbf{x}. \end{aligned} \quad (7)$$

where

$$E^s = \hat{\mathbf{q}} \cdot \mathbf{E}^s, \quad \bar{\mathbf{G}} = \hat{\mathbf{q}} \cdot \mathbf{G}. \quad (8)$$

Here,  $\hat{\mathbf{q}}$  is a unit vector for measuring specific polarization direction.  $\bar{\mathbf{G}}(f, \mathbf{x}_O, \mathbf{x})$  is a projected Dyadic Green's function which converts the vector value  $\hat{\mathbf{p}} \times \mathbf{H}^{\text{inc}}(f, \mathbf{x})$  into a scalar value  $E^s(f, \mathbf{x}_O)$ . The scalar distribution of projected normal vector components  $n^P(\mathbf{x})$  becomes the unknown to be solved. This is termed the scalar formulation of the inverse scattering problem and is similar to the formulation suggested in [31].

### C. Discretization and Matrix Formulation

We set the imaging region and discretize it into a grid. Through the discretization, (7) becomes a linear equation and can be expressed as a relationship between the following matrix and the column vector:

$$E_i^s = \sum_j G_{ij} n_j^P. \quad (9)$$

Here,  $i$  represents the label of the observed data,  $E_i^s$  represents the observed component of the scattered field, which includes specific polarization components at specific observation points and frequencies, and  $j$  represents the label of the grid points in the inverse analysis region. In free space scattering problem, the matrix elements  $G_{ij}$  can be calculated as known quantities from the discretization, Green's function, and physical optics current induced by a given incident field. By aligning the number of grid points in the inverse analysis region with the number of observed data (frequency and spatial sampling), the matrix can

be square, and its inverse can be obtained. Therefore,  $n^p_j$  can be solved from  $E_i^s$ . By plotting the obtained  $n^p_j$  according to the labels of the spatial grid  $j$ , we can obtain an image of the scatterer. By writing  $E^s = \{E_i^s\}$ ,  $n^p = \{n^p_j\}$ ,  $G = \{G_{ij}\}$ , (9) can be written in the matrix notation

$$E^s = G n^p. \quad (10)$$

#### D. Inversion Process With Truncated Singular Value decomposition Regularization

Matrix  $G$  often becomes ill-conditioned, and is susceptible to errors due to the physical optics approximation and measurement errors when considering actual measurements. Therefore, we use truncated singular value decomposition (TSVD) to regularize a solution  $n^p$  of (10) [17], [18]. The singular value decomposition of matrix  $G$  is given by

$$G = U \Sigma V^*. \quad (11)$$

Here,  $U$  is the matrix comprising the left singular vectors  $\{u_i\}$ ,  $V$  is the matrix comprising the right singular vectors  $v_i$ , and  $\Sigma$  is a diagonal matrix with singular values  $\sigma_i$  arranged in descending order as  $\Sigma = \text{diag}(\sigma_1, \sigma_2, \dots, \sigma_i, \dots)$ , and  $V^*$  denotes Hermitian conjugate of the matrix  $V$ . The singular values and left and right singular vectors are given by

$$G v_i = \sigma_i u_i, G^* u_i = \sigma_i v_i. \quad (12)$$

We introduce a truncation threshold  $C = \sigma_{\text{cut}}/\sigma_1$  for the singular values and construct a truncated matrix  $\tilde{\Sigma} = \text{diag}(\sigma_1, \dots, \sigma_{\text{cut}}, 0, \dots, 0)$ . It consists only of singular values equal to or larger than the threshold value  $C$ . Using this matrix, we construct the generalized inverse matrix  $M^+$  as

$$M^+ \approx V \tilde{\Sigma}^+ U^* \quad (13)$$

where  $\tilde{\Sigma}^+ = \text{diag}(1/\sigma_1, \dots, 1/\sigma_{\text{cut}}, 0, \dots, 0)$ . Therefore, the regularized solution of (10) can be obtained by

$$n^p \approx M^+ E^s. \quad (14)$$

This equation can be expressed in following form:

$$n^p \approx \sum_{i=1 \sim \text{cut}} 1/\sigma_i \langle u_i^*, E^s \rangle v_i. \quad (15)$$

Equation (15) can be interpreted as the regularized solution  $n^p$  consisting of a linear combination of the basis  $v_i$  with a coefficient proportional to  $1/\sigma_i$ . The order of the singular values means the contribution significance of scatterer distribution on the scattered field. The smaller singular value components are the smaller contributions to the scattered field. However, in (15), the smaller singular values significantly impact the scatterer distribution. Thus, we can extract the main part of the scatterer's distribution contributing to the scattered field by introducing the truncation of the singular value. This avoids fatal errors caused by the physical optics approximation and measurements through the smaller singular value parts to obtain correct images. This regularization scheme is quite powerful, and its performance has been shown in the literature [17], [18], [19], [20], [21], [22], [23], [25], and [26]. In later sections, we choose the specific truncation threshold empirically to obtain better images for each case.

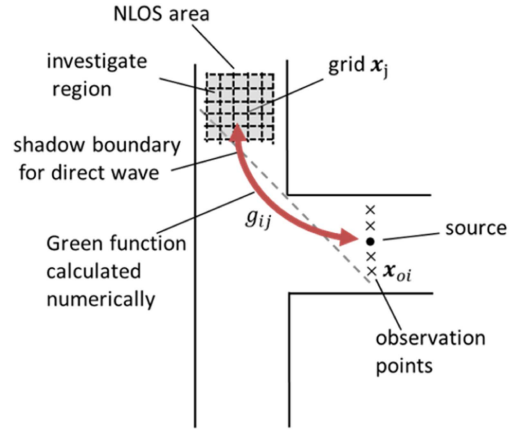


Fig. 3. Conceptual figure of Green's function connecting investigate region and observing points.

### III. APPLICATION TO NLOS ENVIRONMENT

To apply the linearized inverse scattering method with physical optics approximation to the NLOS area, we must consider the geometry of the NLOS environment. Fig. 1 illustrates the geometry of a T-junction comprising PEC walls as the typical geometry of the NLOS environment. We assume that there is a scatterer located in the NLOS area beyond the T-junction, which is the area beyond the line of sight from the transmitting and receiving points. When applying the proposed method to the NLOS area, we cannot use analytically known Green's functions, such as the free-space Green's function, since they do not account for the presence of the walls. Therefore, we must determine the matrix elements in (10), which include information of the walls. In this study, we consider a scenario where the geometry is given, and the structure of the walls is known. We aim to solve the problem of determining the distribution of the scatterer in the presence of these walls. To solve this problem, we first numerically calculate Green's function connecting each point in the NLOS area to the transmitting and receiving points using electromagnetic simulations [22]. This step involves electromagnetic simulations to obtain the Green's function and incident magnetic field for each point in the NLOS area. Using the results of the electromagnetic simulations, we construct matrix  $G$  and solve (10) to image the distribution of the scatterer in the NLOS area. This process is illustrated in Fig. 3. By following this procedure, we can apply the linearized inverse scattering method with physical optics approximation to the NLOS area and obtain an image of the scatterer distribution. This approach allows us to overcome the limitations of using analytically known Green's functions and provides a practical solution for imaging scatterers in complex environments with known wall structures.

This approach's computational complexity can be evaluated as follows: To obtain an accurate image, this method requires full-wave electromagnetic simulation. One of the representative efficient full-wave analysis algorithms is multilevel fast multipole method (MLFMM) [32]. Its computational complexity is known as  $O(N \log N)$ ; here,  $N$  is the number of unknown in forward simulation corresponding to a number of edges of the

TABLE I  
COMPARISON OF COMPUTATIONAL COMPLEXITY

Work	Pre-process	Imaging process	Post-process
This work	Green's function and incident field computations are required to construct matrix $\mathbf{G}$ $O(MN \log N)$ $M$ : number of pixels $N$ : number of edges of geometry model	Solving matrix of pixel number size $O(M^2)$ $M$ : number of pixels	Not required
[7]	Signal modeling and multipath identification are required. If effective reflection paths are restricted, computational complexity is relatively low.	FFT algorithm can be used to obtain images. It leads to relatively lower computational complexity when generating an image with the same number of pixels.	Identification processes of images corresponding to multipath and actual target position are required.
[15]	Signal modeling and multipath identification are required. If effective reflection paths are restricted, computational complexity is relatively low.	FFT algorithm can be used to obtain images. It leads to relatively lower computational complexity when generating an image with the same number of pixels.	- Transformation of virtual image to actual image by mirror symmetry. - High frequency operation requires phase error collection on measured signals to suppress Ghosts images with some gradient or stochastic optimization.

model, and  $N$  scales  $N \propto \lambda^2$ .  $\lambda$  denotes the considered environment dimension measured in analysis wavelength. Therefore, the computational complexity of a single forward analysis is given by  $O(N \log N)$ . To obtain all components of the matrix  $\mathbf{G}$ , we need to repeat the calculation for a number of grid points  $M$ . As a result, the total complexity of forward calculation is  $O(MN \log N)$ . In the imaging process, the complexity is determined by the inversion of the matrix  $\mathbf{G}$  and  $O(M^3)$ . The number of grid points corresponds to the resolution of the image or the number of pixels. In this article, we consider the problem set up  $N \sim O(10^6)$ ,  $M \sim O(10^2)$ . In that case, the imaging process can be negligible, and calculation time is dominated by forward calculation. A qualitative comparison of the computational complexity with typical other approaches reported in [7] and [15] is shown in Table I. Our approach is relatively high computational complexity in the preimaging and the imaging process. However, it can avoid the complex postprocessing step required in other NLOS imaging approaches, such as identifying images related to several multipaths or transforming a virtual image to an actual image, estimating phase error, and modifying it to suppress ghosts in the image. Such procedures sometimes require gradient or stochastic optimization steps. There is an opposability to failure to converge or find a solution. Instead of these, our approach requires a high amount of computation in the preimaging step, but the computation costs are predictable.

Hereafter, considering a 2D problem and a scatterer that is uniform in the  $z$ -direction and limiting the excitation polarization to vertical polarization (along to  $z$ -axis), we have

$\hat{\mathbf{p}} = (\cos \phi^P, \sin \phi^P, 0)$  and  $H_z^{\text{inc}} = 0$ . Therefore,  $\mathbf{H}^{\text{inc}}$  becomes  $\mathbf{H}^{\text{inc}} = (H_{x_j}^{\text{inc}}, H_{y_j}^{\text{inc}}, 0)$ . We also observe the  $z$  component of the scattered field as  $E^s = E_z^s = \hat{\mathbf{z}} \cdot \mathbf{E}^s$ . In this case, given the geometry, we set the imaging region  $D$  and denote the position in the region  $D$  as  $\mathbf{x}_j$  and the transmitting or observing points as  $\mathbf{x}_{oi}$ . Assuming reciprocity between the transmitting or observing points  $\mathbf{x}_{oi}$  and each point in the imaging region  $\mathbf{x}_j$ , we can calculate the numerical Green's function connecting them. To calculate the numerical Green's function, we set a wave source at the transmitting point or one of the observing points  $\mathbf{x}_{oi}$ . We excite the system with the specific polarization, that is intended polarization, with amplitude  $E_0(f, \mathbf{x}_{oi})$ . The numerical Green's function component connecting the current component at the discretized imaging region grid point  $\mathbf{x}_j$  to the transmitting and observing points corresponding to the part of  $\bar{\mathbf{G}}(f, \mathbf{x}_O, \mathbf{x})$  in (8) is denoted as  $g_{ij}$  by  $\bar{\mathbf{G}} = \hat{\mathbf{z}} \cdot \mathbf{G}$

$$g_{ij} = \bar{\mathbf{G}}(f, \mathbf{x}_{oi}, \mathbf{x}_j) = G_{zz} = E_z(f, \mathbf{x}_j) / E_0(f, \mathbf{x}_{oi}). \quad (16)$$

We calculate all components of  $g_{ij}$  for all combinations of  $(i, j)$  by changing the position of the wave source for each observing point. We also set a similar wave source at the transmitting point to obtain the incident magnetic field  $\mathbf{H}^{\text{inc}}(f, \mathbf{x}_j)$ . We have a practical form of (9) to be solved through (16) aswith

$$G_{ij} = g_{ij} (\cos \phi^P H_{y_j}^{\text{inc}} - \sin \phi^P H_{x_j}^{\text{inc}}). \quad (17)$$

#### IV. RESULTS IN NUMERICAL SIMULATION

To verify the effectiveness of this method, we conducted the electromagnetic simulations described in this section.

##### A. Simulation Setup

In the simulation, we focused on imaging the 2D distribution of the target in the plane  $z=0$  m. We set the practical projected direction  $\phi^P = 180^\circ$  (the  $-y$  direction). This corresponds to the direction of the junction center from the imaging area. We used  $n$  grid points and set the length of the observed data to be  $n$ , if the excitation and observing polarizations are the same and have only a  $z$ -component.

With these assumptions, (16) is simplified to the following form:

$$G_{ij} = g_{ij} H_{x_j}^{\text{inc}}. \quad (18)$$

Fig. 4 shows the geometry used in the simulation. We defined a region for inverse analysis NLOS from the transmitting and observing points and placed a PEC object in that region [actually a small part of the area is line-of-sight (LOS) from the observation points, but we considered only cases where the scatterer is completely in the NLOS area as seen from both the source and observing points]. The inverse analysis region is a square with 1 m side lengths centered at  $(x, y) = (0, 2)$  m, and is discretized with a grid of  $21 \times 21$  points with a spacing of 0.05 m in both the  $x$  and  $y$  directions. We set the observation conditions to match the number of grid points. The coordinate origin is set at the center of a T-junction, and there is only one transmitting point at  $(x, y) = (2, 0)$  m. Only the electric field's  $z$ -component was excited at this point.

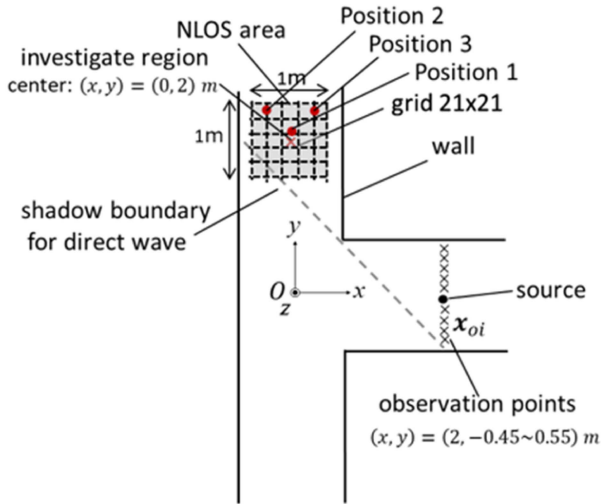


Fig. 4. Geometry used in simulation.

 TABLE II  
 SIMULATION SETUP

Target Scatterer	PEC plate 1 m high 0.3 m wide PEC cylinder with height 1m diameter 0.3 m PEC plate 1 m high 0.6 m wide
Frequency	2.0-2.96 GHz, 0.02 GHz steps, 49 points
Imaging region and discretization	$x = -0.5$ to $0.5$ m, 0.05 m steps, 21 points $y = 1.5$ to $2.5$ m, 0.05 m steps, 21 points in total 441 grid points
Transmitting point	$(x, y) = (2, 0)$ m
Observing points	$(x, y) = (2, -0.45)$ m, $(2, -0.35)$ m, $(2, -0.25)$ m, $(2, -0.15)$ m, $(2, 0.15)$ m, $(2, 0.25)$ m, $(2, 0.35)$ m, $(2, 0.45)$ m $(2, 0.55)$ m
Polarization	Parallel to the $z$ -axis

The observation points were set at  $(x, y) = (2, -0.45)$  m,  $(2, -0.35)$  m,  $(2, -0.25)$  m,  $(2, -0.15)$  m,  $(2, 0.15)$  m,  $(2, 0.25)$  m,  $(2, 0.35)$  m,  $(2, 0.45)$  m,  $(2, 0.55)$  m and we obtained the  $z$ -component of the scattered field. The frequency range was from 2.0 to 2.96 GHz with steps of 0.02 GHz, resulting in 49 points. Thus, giving 441 points in total, which matched the number of grid points. We performed three types of simulations to compare and verify the effects of changes in the position, shape, and size of the scatterer. At first, we varied the position of a PEC plate 1 m high and 0.3 m wide. Next, we varied the shape of PEC scatterers cylinder with a height of 1 m and a diameter of 0.3 m. Finally, we compared two PEC plates with heights of 1 m and widths of 0.3 and 0.6 m located in the center to test the capability of detecting size changes in scatterers. The settings and parameters for each measurement case are summarized in Table II.

For the forward analysis in the simulations, we used the MLFMM solver in the FEKO commercial electromagnetic simulator. Fig. 5 shows an example of a 3D model used in the

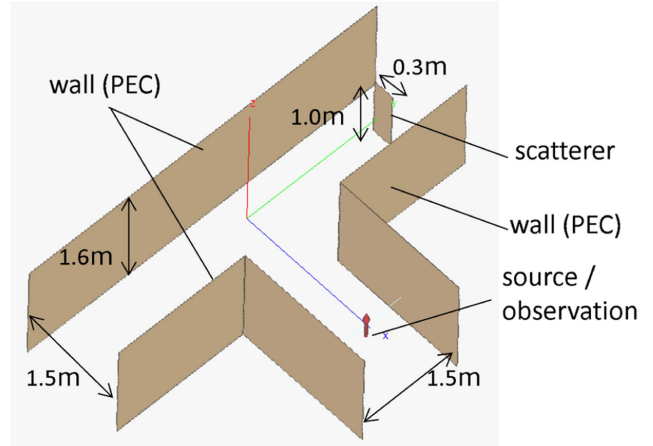


Fig. 5. 3D geometry model used in the simulations.

simulations. We constructed a T-junction comprising walls 1.6 m high. The transmitting wave source was placed in front of the T-junction, and the scatterer was placed in a location where it obstructed the LOS from both the transmitting and observation points. In this setup, both the wall of the T-junction and the scatterer were assumed to be perfect electric conductors (PECs). In these simulations, we used an infinitesimal electric dipole along the  $z$ -axis as an omnidirectional wave source on the observation plane. For simplicity, we did not consider the presence of a floor. In actual environments, there may be multipath components caused by the floor, but their contributions would be considered smaller and less dominant than those of the planar propagating components. Furthermore, when considering actual radar observations, beamforming toward the observation plane is expected to further reduce the influence of the floor. We check this assumption through simulations for a model with a floor in Appendix A. The influence of the floor's existence does not cause significant deviation from the image. When we apply the vertical beam-forming antenna pattern, the resulting image gets closer to the image of the model without the floor.

### B. Simulation Procedure

The simulation was conducted by following these steps.

1) *Creating the Geometry Model*: Create a 3D model for the electromagnetic simulation corresponding to the geometry shown in Fig. 5 (Fig. 5 shows an example).

2) *Calculating the Matrix Components of  $G$* : Calculate the numerical Green's function and the incident magnetic field to obtain matrix  $G$ . In this process, the response between all combinations of grid points in the inverse analysis region and the transmitting/observing points is calculated using (9), and the components of matrix  $G$  were computed using (11).

3) *Generating the Input Data*: The scattered field  $\mathbf{E}^s((f, \mathbf{x}_o)_i)$  at each observation point when a scatterer is present was calculated as the verification input data. Here,  $\mathbf{E}^s((f, \mathbf{x}_o)_i) = \mathbf{E}^{\text{scat}}((f, \mathbf{x}_o)_i) - \mathbf{E}^{\text{bkg}}((f, \mathbf{x}_o)_i)$ , where  $\mathbf{E}^{\text{scat}}((f, \mathbf{x}_o)_i)$  is the electric field at observation point  $\mathbf{x}_{oi}$  obtained when a scatterer is present and the omnidirectional

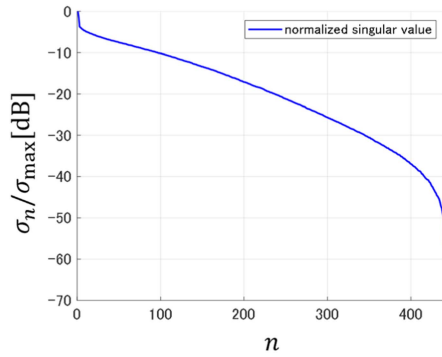


Fig. 6. Distribution of singular values. The vertical axis represents normalized singular values expressed in dB.

wave source at the transmitting point is excited at frequency  $f$ , and  $\mathbf{E}^{\text{bkg}}((f, \mathbf{x}_o)_i)$  is the electric field at observation point  $\mathbf{x}_{oi}$  obtained when the scatterer is absent and the omnidirectional wave source at the transmitting point is excited at frequency  $f$ .

4) *Executing Inverse Analysis:*  $\mathbf{E}^{\text{s}}((f, \mathbf{x}_o)_i)$ , obtained from the simulation as input data for the inverse analysis, is used to solve (9) following the TSVD method described in Section II-D to obtain the distribution  $n^{\text{p}}(\mathbf{x}_j)$ . The obtained  $n^{\text{p}}(\mathbf{x}_j)$  may be complex due to errors, although it is originally a real number. Therefore, the absolute value of  $n^{\text{p}}(\mathbf{x}_j)$  is taken and normalized by the maximum value  $\overline{n^{\text{p}}_j} = |n^{\text{p}}_j| / \max(\{|n^{\text{p}}_j|\})$  and is plotted according to the spatial label  $j$ .

### C. Simulation Results

The results of the simulation are presented further. First, the distribution of singular values obtained by performing singular value decomposition on matrix  $\mathbf{G}$  calculated in Step 2) is shown in Fig. 6. The blue line represents the distribution of singular values normalized by the maximum singular value. In this simulation, the truncation threshold for the singular values  $C = 10\log_{10}(\sigma_{\text{cut}}/\sigma_1)$  was set to around  $-15$  dB, and inverse analysis was performed. The comparison and verification results for the cases where the position, shape, and size of the scatterer varied are presented further.

1) *Evaluation of Resolution:* We evaluate the system resolution through imaging of a PEC sphere with a diameter of 0.05 m, which is comparable to the grid distance of 0.05 m, placed at the center of the NLOS imaging area  $(x, y) = (0, 2)$  m, as a point-like target. Fig. 7 shows the results. Fig. 7(a) represents the result of the image and its distribution concentrates on the target marked dashed white circle. Fig. 7(b) and (c) represents sectional distribution properties corresponding to a point spread function on the line  $y = 2.0$  m (b), and  $x = 0$  m (c). A half width of the sectional profile denoted both-side-arrow in the figure is 0.06 m for  $x$  direction, and 0.11 m for  $y$  direction.

We also check separation resolution in cases with multiple targets in the imaging area. Fig. 8 shows imaging results for a pair of thin PEC cylinders with a diameter of 0.05 m and height of 1.0 m placed at relative center  $(x, y) = (0, 2.15)$  m with separation along the  $x$  direction. Fig. 8(a), (c), (e) represents results of

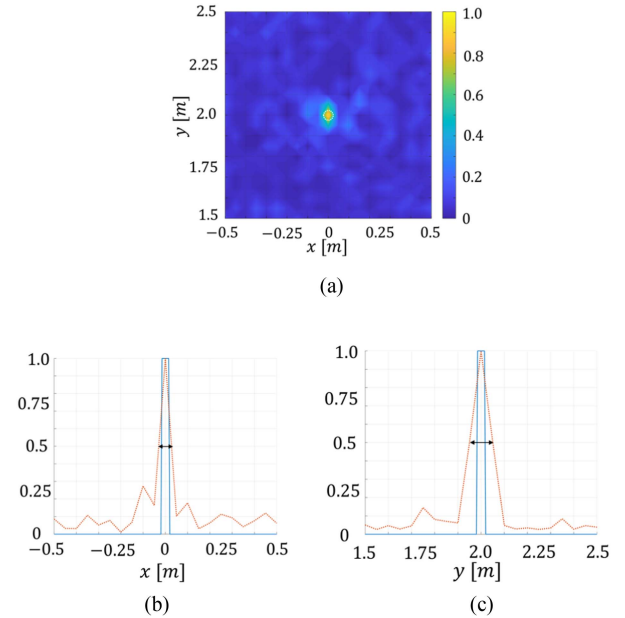


Fig. 7. Evaluation results of image resolution for the PEC sphere with diameter 0.05 m as a point like target placed at the center of the NLOS imaging area. (a) Image. (b) Sectional distribution property corresponding to the point spread function on the line  $y = 2.0$  m. (c) Sectional distribution property on the line  $x = 0$  m. The singular value truncation threshold  $C$  is set to  $-15$  dB in this case.

image for separation distances 0.1, 0.3, 0.6 m, respectively, and Fig 8(b), (d), (f) represents sectional distribution properties for each separation. The physical optics approximation cannot correctly deal with multiple reflections between the multiple targets, which the vertical extent of the target may produce, however if the separation of the target was sufficiently large (the separation larger than 0.3 m), the result of the image resolved independent multiple targets.

2) *Variation of Scatterer Position:* The results for a PEC plate with a width of 0.3 m are shown in Fig. 9. Three different plate position cases are considered: Position 1, Position 2, and Position 3. Position 1 denotes the case where the plate was placed along to  $x$  direction with its center at  $(x, y) = (0, 2.15)$  m. Position 2 denotes that the same plate was set at  $(x, y) = (-0.3, 2.3)$  m. Position 3 means that the same plate was set at  $(x, y) = (0.3, 2.3)$  m. Fig. 9(a) represents position 1, Fig. 9(b) represents position 2, and Fig. 9(c) represents position 3. The dashed white rectangle indicates the true position and extent of the scatterer, and the image of the scatterer is localized around the true position. Fig. 10 shows the characteristics of the scattered field obtained in the Position 1 case. Fig. 10(a) shows the frequency characteristics of the scattered field at observation point  $\mathbf{x}_o = (2, -0.25)$  m, and Fig. 10(b) shows the spatial characteristics at  $f = 2.54$  GHz. The blue line represents the calculated scattered field based on the true distribution of the scatterer using (9), the dashed black line represents the numerical analysis values used as input for the inverse analysis, and the dashed red line represents the calculated scattered field based on the distribution obtained from the inversion result through (9). Each line corresponds to the respective case, and the results of the inverse analysis accurately reproduce the input values.

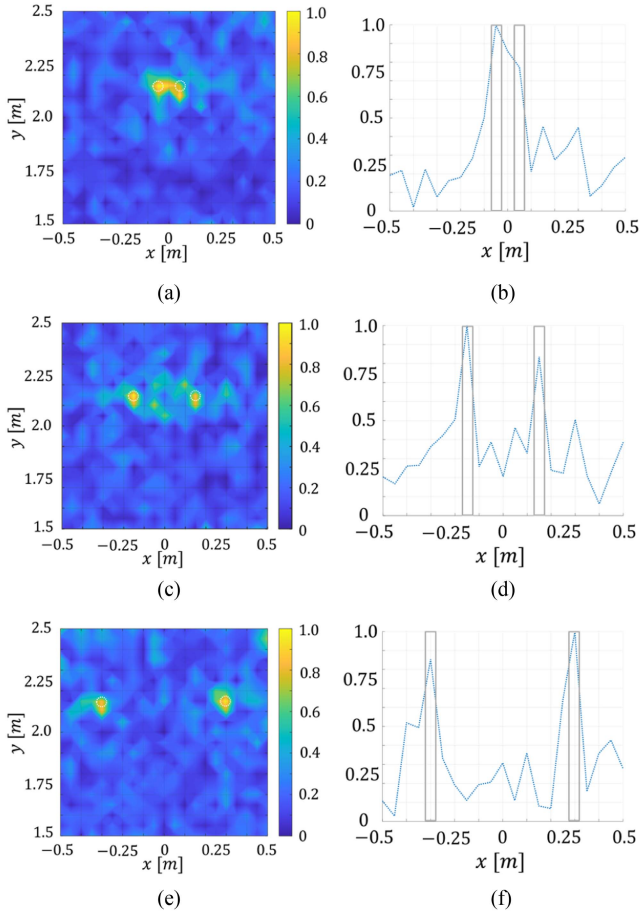


Fig. 8. Evaluation results of image separation for the multiple targets. The images of the pair of cylinders with separation along to  $x$  direction (a) 0.1 m, (c) 0.3 m, (e) 0.6 m. Sectional distribution properties on the line  $y = 2.15$  m for separation distance (a) 0.1 m, (c) 0.3 m (e) 0.6 m. The true position of the cylinders is marked white dashed circles and gray bars. The singular value truncation threshold  $C$  is set to  $-11$  dB in this case.

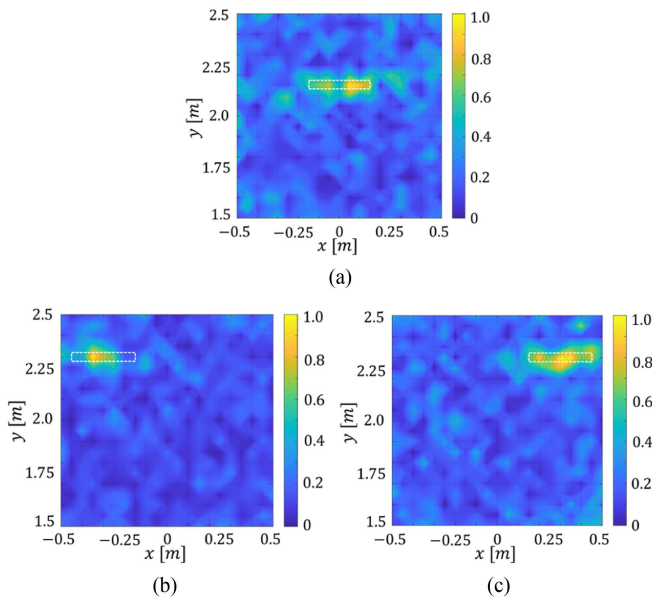


Fig. 9. Imaging results of the PEC plate for position variation. (a) Position 1. (b) Position 2. (c) Position 3. The broken white line denotes a true object boundary.

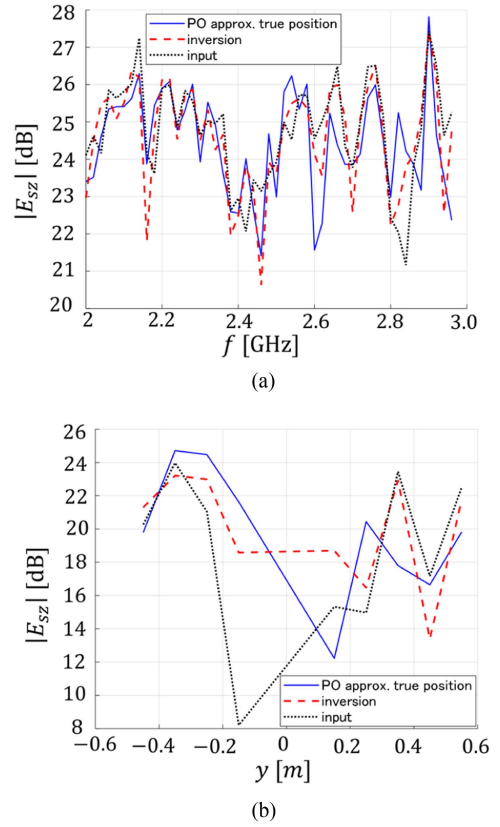


Fig. 10. Comparison of scattering properties in the result for Position 1. (a) Frequency characteristics at  $\mathbf{x}_o = (2.0, -0.25)$  m. (b) Spatial characteristics on the observation points at  $f = 2.54$  GHz.

3) *Variation of Scatterer Shape*: We tested the imaging method's performance on the metal cylinder, which is a typical scatterer with curved surfaces. The metal cylinder has a height of 1 m and a diameter of 0.3 m and is placed in the same center positions as the metal plate cases' Positions 1, 2, and 3. In this regard, the cylinder's symmetric axis directs the  $z$ -axis. Fig. 11 shows the obtained images. In Fig. 11, panels (a) to (c) represent positions 1 to 3. The truncation criteria  $C$  was chosen, respectively, at  $-15$ ,  $-14$ , and  $-12$  dB, to obtain better images. The obtained distributions correspond to the extent of the illuminated side of the true cylinder expressed as the dashed white circle. The broken white line denotes a true object boundary.

4) *Variations in Scatterer Size*: We compare the cases when the 0.3 m wide metal plate was placed along to  $x$  direction with its center at  $(x, y) = (0, 2.15)$  m (Position 1), and when the 0.6 m wide metal plate was placed along to  $x$  direction with its center also at Position 1. Fig. 12 shows the obtained images. Fig. 12(a) represents the 0.3 m wide plate, which is the same as Fig. 9(a), and Fig. 12(b) represents the 0.6 m wide plate. The region where the distribution is concentrated changes, indicating that the width of the metal plate is being captured.

5) *Effects of Adding Noise*: To investigate the robustness to the effect of noise, we examined the case where noise with randomly assigned amplitude and phase was added to the scattering field data used as input for imaging. The noise was added by

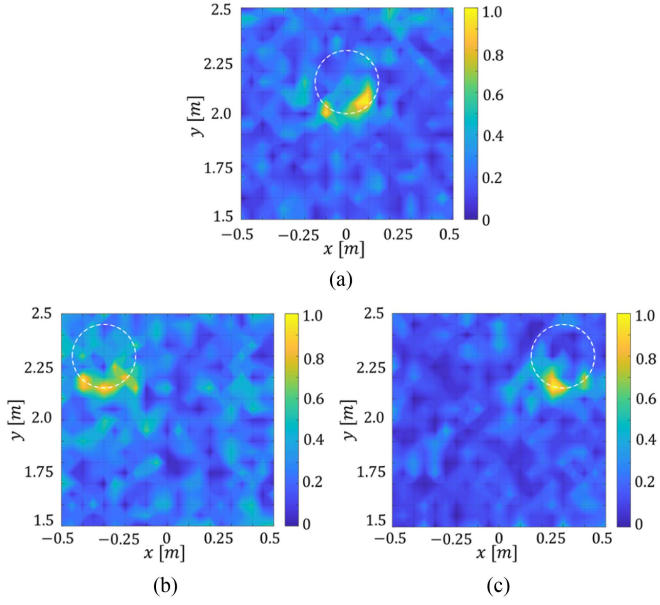


Fig. 11. Imaging results of the cylinder for scatterer shape comparison. (a) Position 1 with  $C = -15$  dB. (b) Position 2 with  $C = -14$  dB. (c) Position 3 with  $C = -12$  dB. The broken white line denotes a true object boundary.

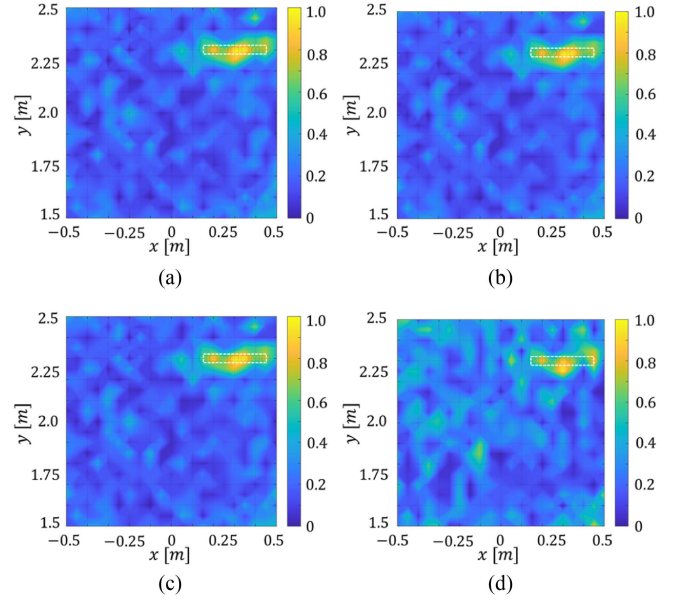


Fig. 13. Comparison of imaging results for adding noise on position 3 scattering data. (a) Without noise. (b)  $S/N=20$  dB,  $C > N$ . (c)  $S/N = 15$  dB,  $C \approx N$ . (d)  $S/N=6$  dB,  $C < N$ .

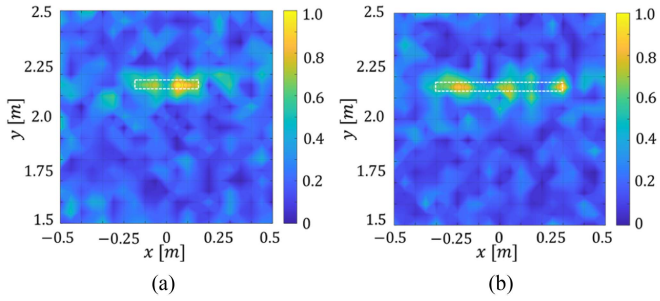


Fig. 12. Comparison of imaging results for scatterers of varying sizes. (a) Plate 0.3 m wide. (b) Plate 0.6 m wide. The broken white line denotes a true object boundary.

setting the  $S/N$  ratio based on the maximum amplitude of the field, and the changes in images due to different  $S/N$  values were compared. The results for the PEC plate with a width of 0.3 m placed at position 3 are shown in Fig. 13. Fig. 13(a) represents the case without noise [same as Fig. 9(c)], Fig. 13(b) represents the case with an  $S/N$  of 20 dB, where the noise level is lower than the truncation threshold of the singular values  $C = -15$  dB, Fig. 13(c) represents the case with an  $S/N$  of 15 dB, where the noise level is around the truncation threshold of the singular values, and Fig. 13(d) represents the case with an  $S/N$  of 6 dB, where the noise level is higher than the truncation threshold of the singular values. In Fig. 13(a)–(c), there are only little changes in the images, indicating that stable imaging can be achieved as long as the noise level is equal to or below the truncation threshold of the singular values. In Fig. 13(d), the image is more spread out, and positions away from the true scatterer location are also brighter. However, strong values are concentrated near the center of the scatterer. Thus, imaging

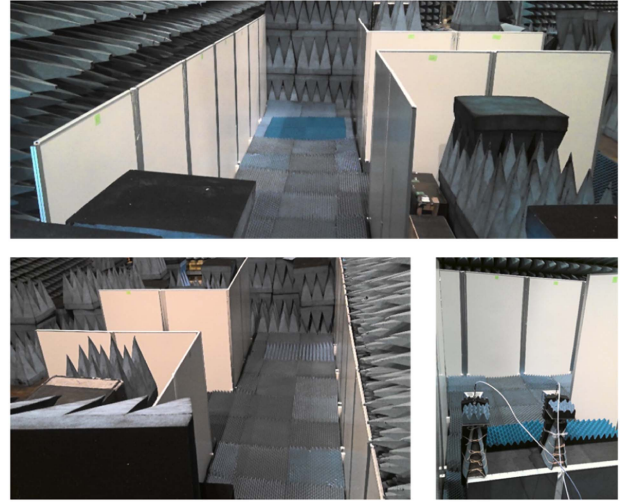


Fig. 14. Views of the T-junction geometry used in the experiment.

target located in the NLOS region is still possible under the environment with existing noise.

## V. RESULTS IN EXPERIMENT

To verify this method's feasibility, we conducted an indoor experiment using a T-junction geometry comprising metal walls in an anechoic chamber.

### A. Experiment Set-Up

Fig. 14 shows the T-junction geometry used in the experiment. It comprised a metal wall passage approximately 1.5 m wide and approximately 1.6 m high, corresponding to the simulation.

TABLE III  
 EXPERIMENT SET UP

Target Scatterer	#1 Metal plate 0.2 m high 0.3 m wide #2 Metal plate 0.2 m high 0.6 m wide #3 Metal plate 1 m high 0.3 m wide #4 Metal plate 1 m high 0.6 m wide
Frequency	2.0–3.0 GHz, 0.005 GHz steps, 201 points
Imaging frequency	2.0–2.24 GHz, 0.005 GHz steps, 49 points
Imaging region and discretization	$x = -0.5$ to $0.5$ m, $0.05$ m steps, 21 points $y = 1.5$ to $2.5$ m, $0.05$ m steps, 21 points in total 441 grid points
Transmitting point	$(x, y) = (2, 0)$ m
Observing points	$(x, y) = (2, -0.45)$ m, $(2, -0.35)$ m, $(2, -0.25)$ m, $(2, -0.15)$ m, $(2, 0.15)$ m, $(2, 0.25)$ m, $(2, 0.35)$ m, $(2, 0.45)$ m $(2, 0.55)$ m
Polarization	Parallel to the $z$ -axis

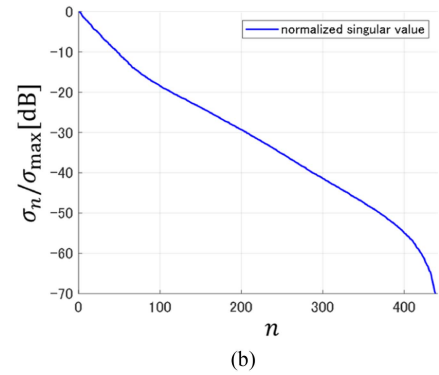
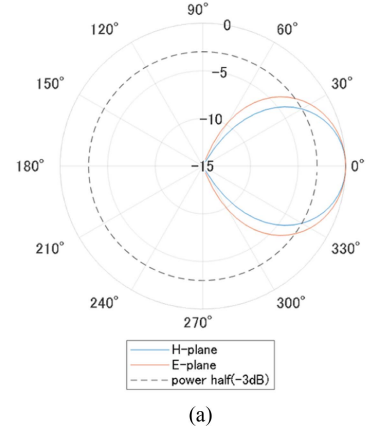


Fig. 15. Radiation pattern used in the forward calculation and resulting singular value distribution of matrix  $\mathbf{G}$ . (a) Antenna's radiation pattern with beamwidth  $60^\circ$  in the H-plane and  $67^\circ$  in the E-plane. The angles denote the elevation and azimuth angles measured from the antenna's boresight. (b) Singular value distribution expressed in dB in the measurement setup.

The walls were constructed by arranging aluminum partitions in indoor environments such as offices. The seams between neighboring partitions were sealed with aluminum tape. The floor was covered with absorbers to suppress the occurrence of multipath components. This is because irregular reflections from the floor are expected in this experimental configuration because the formation of the elevation direction beam is not considered. The transmitting antenna was installed in the middle of the passage, 2 m in front of the T-junction's center, where the coordinate originates. The nine observation points spanned the passage 2 m in front of the T-junction at the same  $x$  position as the transmission point, avoiding any overlap with the transmitting antenna. The antenna used in the experiment was a double ridge horn (FT-RF, model HA-0218G-NF) for both transmission and reception. The Keysight network analyzer N9918B was used for signal generation and reception, and the frequency characteristics were obtained by employing a linear step sweep. The experimental setup is shown in Table III.

In calculating the matrix components for the imaging process and the incident field, we consider the radiation pattern corresponding to the antenna used in the experiment. Fig. 15(a) shows the antenna pattern, and Fig. 15(b) shows the singular value distribution of the resulting matrix. We evaluate the system resolution of the measurement set up in Appendix B.

Fig. 16 shows the experimental scatterers. Imaging processing was performed for four types of scatterers, combinations of heights of 0.2 and 1 m, and widths of 0.3 and 0.6 m, when placed in the center of the imaging region. The white part of the target scatterers was styrene foam, which supported the target's position. The foam's contribution to scattering can be ignored. The gray part is aluminum, which serves as the test target.

### B. Experimental Results

Fig. 17 shows an example of the experimental received signal. It represents the range profile of the  $1 \text{ m} \times 0.3 \text{ m}$  metal plate

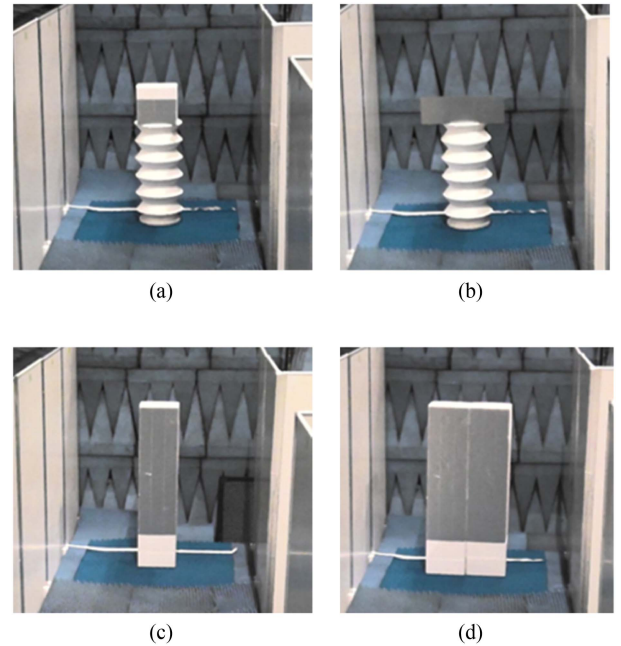


Fig. 16. Metal plates used in the experiment as the target scatterer. (a) Height 0.2 m width 0.3 m. (b) Height 0.2 width 0.6 m. (c) Height 1 m width 0.3 m. (d) Height 1 m width 0.6 m.

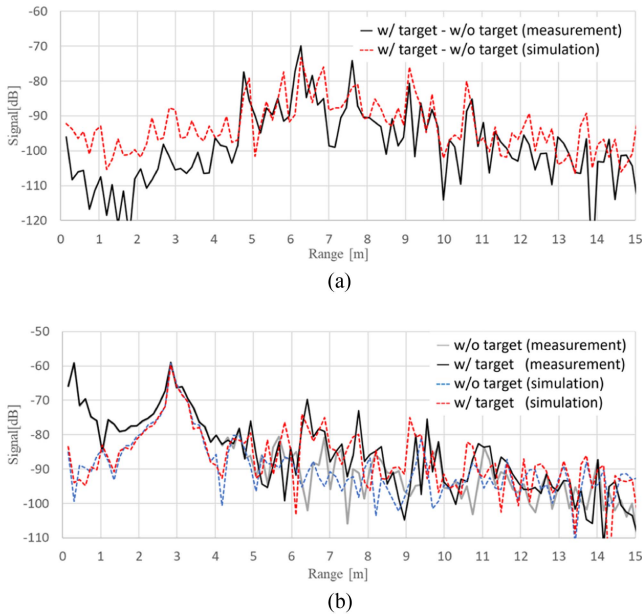


Fig. 17. Range profile of the background geometry and NLOS scatterer. (a) Measured and simulated range profiles for the background and the NLOS target. At approx. 0.3 m, there is a mutual coupling between the Tx and Rx antennas. At approx. 2.8 m, there is a dominant signal from the wall opposite the Tx and Rx antennas. After that, we found signals from the NLOS target mainly through the multipath propagation component. (b) NLOS target's measured and simulated range profiles after background subtraction.

[Fig. 16(c)] placed at Position 1 (0, 2.15) m obtained by the inverse Fourier transform of the frequency response acquired at the receiving point (2, 0.15) m. Fig. 17(a) shows the range profile of the background walls without a target and the range profile of the target located in the geometry. The solid line denotes the experimental values, and the dashed line denotes the FEKO simulation results with the directive wave source shown in Fig. 15(a). In this case, since no calibration was based on measuring the calibration target, the experimental values and simulation values were normalized and displayed so that the maximum values match. In the experimental values, a coupling between the transmitting and receiving antennas is observed near 0.3 m, and a response from the wall in front of the transmitting and receiving antennas is observed near 3 m. Beyond that, a more substantial response is observed when the scatterer is present than from the background walls alone. This response can be attributed to multipath components originating from the scatterer in the NLOS area. Fig. 17(b) shows the range profile with the background subtraction. Beyond 4 m in the NLOS area, the characteristics of the experimental and simulation values correspond well, indicating that a signal from the NLOS area could successfully be obtained from the multipath components. The imaging signal is derived by gate processing, which extracts only the signal corresponding to the 4–10 m range from the acquired wide-band signal. This suppresses unnecessary components from outside the experimental geometry.

The imaging process utilized data from nine observation points and 49 frequency points ranging from 2.0 to 2.24 GHz, at intervals of 0.005 GHz, after gate processing. At this time, there

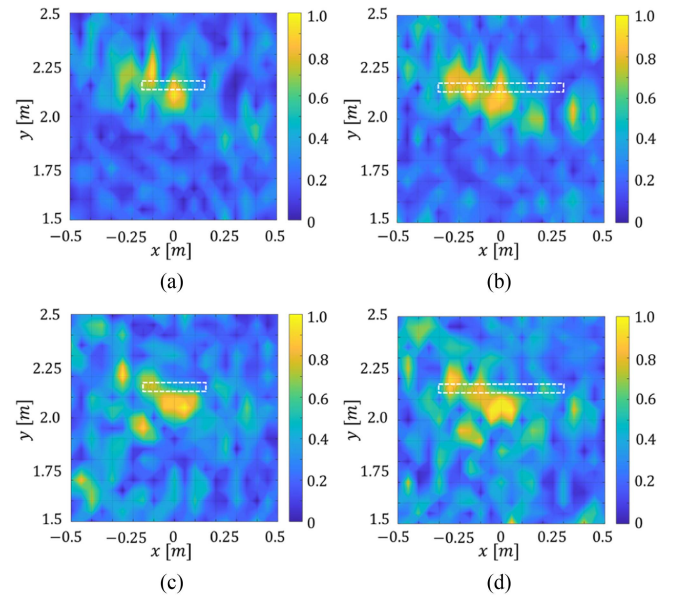


Fig. 18. Imaging results for the test target plates. (a) 0.2 m  $\times$  0.3 m. (b) 0.2 m  $\times$  0.6 m. (c) 1 m  $\times$  0.3 m. (d) 1 m  $\times$  0.6 m. The broken white line denotes a true object boundary.

is potentially a 10 cm order error in the geometry construction. Adjustments to the geometry were considered in calculating matrix  $G$  to match the data obtained from the experiment. The model used to calculate matrix  $G$  for the imaging process assumes a passage width of 1.6 m. Phase delays caused by the displacement of the phase center of the transmitting and receiving antennas and the cable length were corrected at each observation point by assuming the location error and cable length. Additionally, the truncation threshold  $C$  of the singular value shown in Fig. 15(b) during the imaging process was set to  $-8$  dB in the experiment.

Fig. 18 shows the imaging results. The top row shows the images of a metal plate 0.2 m high, (a) representing widths of 0.3 m, and (b) 0.6 m. In both cases, the image distribution concentrated around the actual target position described by the dashed white box. Comparing (a) and (b), the image of the wider scatterer (b) is spread wider along the scatterer's extending direction than (a), and the distribution extends according to the size of the target. The bottom row of Fig. 18 panels (c) and (d) shows the imaging results for targets 1 m  $\times$  0.3 m and (c), 1 m  $\times$  0.6 m. In both cases, the main distribution is concentrated near the actual target position. The image also extended according to the width of the target. However, we realized that the method is sensitive to the alignment and approximation error. In the future, we will take a more robust approach during the matrix inversion.

### C. Discussion

We remark here on issues found in our investigation and the possibilities of solving them in further study in future work.

1) *Errors in Results of the Simulation and Experiment:* In the T-junction, geometry may produce an area where the incident field distribution is weak, such as a standing wave node in the waveguide, by superposition of multiple-bounced waves. A

TABLE IV  
COMPARISON WITH OTHER STATE-OF-THE-ART WORKS

Work	Approach	Frequency	Image Dimension	Geometry	Target	Priori Information	Range	Simulation	Experiment
This work	Inverse scattering + TSVD + primary direction projection	2-3 GHz	2-D	T-junction	2-D Object shape	Known geometry	~5 m	3-D model	Ideal indoor environment
[22]	Inverse scattering + TSVD	1-2 GHz	2-D	Open junction	2-D cylinder	Known geometry	~1 m	2-D model	Non
[4]	FMCW SIMO + Phase difference detection	23.75-24.25 GHz	time trajectories of points	L-corner	Human localization	Known geometry	~7 m	Non	Real indoor environment
[7]	Back Projection + hypothesis matching	0.6-1.4 GHz	2-D	L-corner	Human localization	Partially unknown wall	~10 m	2-D model	Real indoor environment
[15]	MIMO + Minimum entropy focus + Mirror symmetry back projection	77 GHz	3-D	Isolating wall and mirror wall	Complex 3-D object shape	Partially unknown wall	~1 m	3-D model	Ideal indoor environment

portion of the target located at that point could not be captured in a resulting image by physical optics approximation based on this method. Extending the operation frequency band to a higher frequency or adding more space observation points could mitigate the standing wave-like effect. In higher operation frequency, the computational cost of this approach increases, and geometry alignment sensitivity may also increase. These require more computational resources and an additional mitigation strategy to obtain precise geometry structure or compensate for the effect of deviation of the model used for forward calculation from the actual geometry.

2) *Limitation of Our Approach*: In our specific formulation, we solve the component of the normal vector projected on the primal direction of energy transfer. A target parallel to the primal energy transmitting direction might fail to image in this method. Such an object can be difficult to image or detect even in any other approach because it does not have sufficient cross-section to produce a scattered field observed by the radar.

For nonmetallic objects, if the object is low-dielectric material, this method may fail to capture the target. However, supposing the object of high dielectric or high conductivity material, this method may capture the object's shape by a scattering field similar to that of a metallic object. The human body is approximated well as PEC objects even in the similar frequency band of this work reported in [28] and [29]. For a target consisting of partially reflective objects, this method may be able to capture a portion of the target, such as the multiple target cases shown in the first part of Section III-C.

As away from the endpoints or discontinuous points of the wall, angled multipath components corresponding to higher order waveguide modes in the field between the walls decrease. It leads to resolution degradation in the far region from the junction and fails to resolve the image in faraway areas. We confirmed this behavior quantitatively in Appendix C. When our approach is applied, the imaging area should be set sufficiently close to the area bounded by the walls making the NLOS environment. Moreover, in such likely cases, the geometry model becomes large to image a far area. It leads to higher computational costs, which may become a practical limit of this approach.

3) *Clutter Mitigation Strategy and Truncation Determination*: In the experiment, we applied time gate processing on the measured data for the signal range, which is supposed to be relevant for the imaging area before the imaging process. The gating process can mitigate the clutters outside the imaging area. In the last part of Section III-C, the TSVD regularization was performed to suppress the influence of random clutters. In this article, the truncation threshold for the singular values is selected empirically to obtain a better image so that a sufficiently large number of singular components contribute to reproducing the target distribution.

4) *Other Regularization Candidates*: There are several candidates for regularization or robust approach to the matrix inversion and solutions for issues discussed above. One applies the  $l_1$  norm regularization [33], [34]. The metallic surface distribution in our NLOS problem setup could be sparse and  $l_1$  norm regularization is well-suited to solving this kind of problem. Another approach is to apply the total variation method [35]. In our problem setup, the image of the metallic scatterer can be captured as discontinuities between the blank background and the scatterer surface. This makes the total variation method suitable for extracting such discontinuities. Additionally, we can extend the method presented in this article to arbitrary 2D-shaped scatterer imaging by doubling the length of the observation data and expanding matrix  $\mathbf{G}$  to  $2N \times 2N$  [as opposed to (9)]. This could provide more robust and precise images by doubling the quantity of information.

5) *Challenges Toward 3D Reconstruction*: A direct 3D reconstruction of an arbitrary object by the inverse scattering approach considered in this article could be possible in principle. However, it leads to a much larger number of conditions of the matrix and requires much more computation, for example, at least several times as this work. Therefore, obtaining a regularized solution is expected to be quite hard. On the other hand, there are practical possibilities to achieve 3D reconstruction by accumulating a 2D slice strategy with a beam forming at different observation planes. This approach reduces the complex coupling caused in the additional direction by beam forming on each slice. It can also utilize the 2D formulation verified in this work.

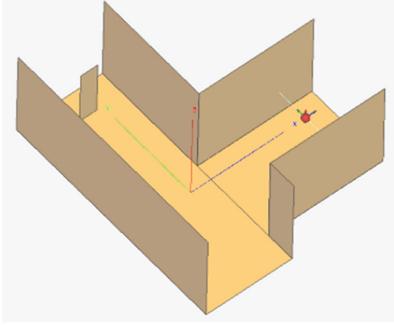


Fig. 19. Simulation model for evaluation of floor influence.

6) *Comparison With Other Approaches:* We summarize a comparison with the achievement of this work and other state-of-the-art NLOS imaging works. Table IV shows a summary of the comparison. This work can be characterized by lower operation frequency and dealing with a medium range, relatively compared to other works. A distinctive feature of this work is the first experimental verification of the inverse scattering approach enabled by the primal direction projection. One of the advantages of our approach is that the method is comprehensively applicable to different NLOS geometry if the geometry information is known. Other works heavily depend on the specific geometry setup, and when the type of geometry changes, the signal model used in the method should be reconstructed, and their algorithms might require modification.

## VI. CONCLUSION

We investigated the multipath exploitation-based inverse scattering method for imaging NLOS targets. In the problem setup where a T-junction is assumed, and the geometry of the environment is known, we numerically obtained Green's function, which connects the observation points and the imaging region and contains multipath propagation components. By constructing a matrix to represent the scattering properties and applying singular value decomposition to determine the distribution of scatterers, we imaged the scatterers located in the NLOS area. We considered the practical formulation of the method to adopt typical NLOS scenario as 2D planar imaging. We verified the method through simulations using a 3D model, which confirmed that the obtained distribution corresponds to the position and size of the scatterers in the 2D plane. We also conducted an experimental feasibility test of the method in an anechoic chamber. We confirmed that the localization and image distribution corresponded to the extent of the scatterer's actual position in the NLOS area. This confirmed the efficacy of this method for imaging the NLOS area.

## APPENDIX

### A. Floor Influence on Image

We check the assumption that the influence of the floor's existence can be negligible or mitigated by vertical beam forming through simulations for a model with the floor. Fig 19 shows the

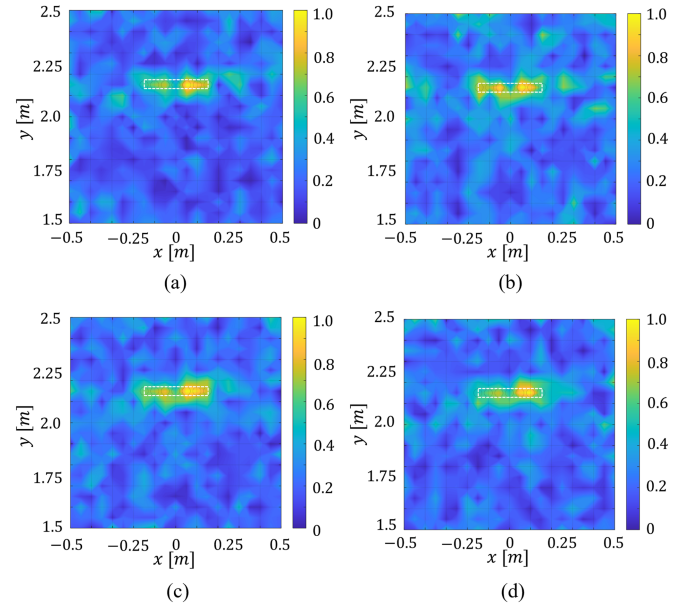


Fig. 20. Evaluation results of the influence of the floor's existence on images. (a) Model without floor. (b) Model with floor excited by the dipole source. (c) Model with floor excited by the source with omni-directive on the imaging plane and vertical beam forming with the half beam width  $6^\circ$ . (d) Model with floor and the same beam pattern as the experiment. The truncation threshold of the singular value is set to  $-15$  dB, the same as the main text case.

simulation model with the floor, where the whole model consists of PEC, and the opposite side to the target of the T-junction is ignored (we confirmed that this portion does not contribute to the target's scattered field). We performed the simulation for this model with floor, and the obtained data are used to input data for the imaging process. The forward calculation part of the process is common with the floorless cases in the main text. Fig. 20 shows the results. Fig. 20(a) represents the image for the floorless case reported in the main text, (b) represents the image for the model with floor and the electric dipole excitation, (c) represents the image for the model with floor and omni-directive on the imaging plane and vertical beam forming antenna pattern with the half beam width  $6^\circ$ , and (d) represents the image for the model with floor and the same beam pattern as the experiment in the main text. As a result, the influence of floor existence does not cause significant deviation in the image by comparing (a) and (b), and when we apply the vertical beam forming pattern, the resulting image gets closer to the image of the model without a floor, by comparing (a) and (c). Therefore, our assumption is justified in this case.

### B. Evaluation of Resolution in Experiment Set-Up

We check the system's resolution in the experiment set-up through simulation for the imaging of the PEC sphere with a diameter of 0.05 m. The target is the same as the main text simulation, but observation parameters are different, that is, the frequency band, the beam pattern, and the singular value truncation threshold. The results are shown in Fig. 21. Fig. 21(a) represents the result of the image, and its distribution concentrates on the target marked dashed white circle. Fig. 21(b) and (c) represents

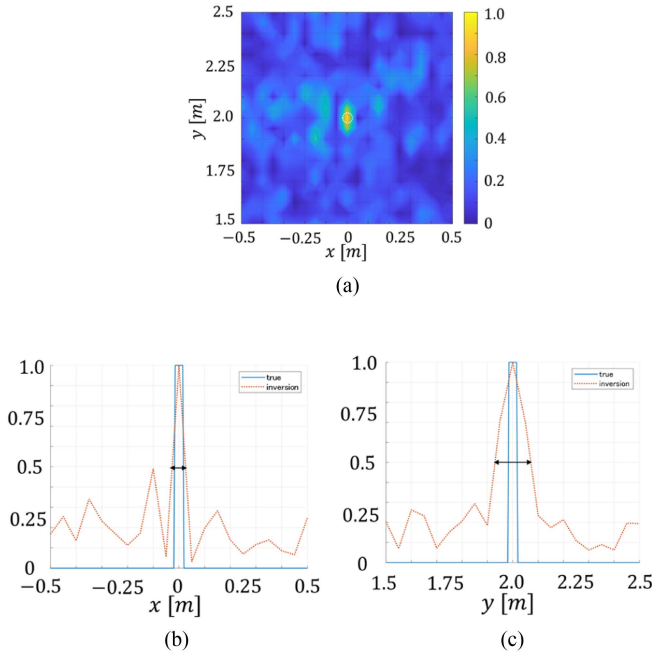


Fig. 21. Evaluation results of image resolution for the PEC sphere with a diameter of 0.05 m were placed in the NLOS area in the experiment setup. (a) Image. (b) Sectional distribution property corresponding to the point spread function on the line  $y = 2.0$  m. (c) Sectional distribution property on the line  $x = 0$  m. In this case, the singular value truncation threshold  $C$  is set to  $-8$  dB.

sectional distribution properties. A half-width of the sectional profile denoted as the both-side-arrow in the figure is 0.06 m for the  $x$  direction and 0.16 m for the  $y$  direction. Compared to the main text case, the  $y$  direction resolution and contrast of the image are degraded. Reasons for these can be considered as follows: the  $y$  direction resolution could be dominated by the range resolution of a conventional radar in free space. We use a narrower bandwidth in the experimental setup than the main text. The result might reflect this aspect. The contrast degradation could be caused by a sharper-shaped beam than the main text. The number of contributing paths decreased, and the scattered field strength from the weak target was lowered. As a result, the S/N in the experimental setup decreased, and the image contrast degraded. However, the system resolution keeps the capability to capture the extent of the target in the NLOS area.

### C. Evaluation of Resolution in Distance Changes

We evaluated the dependence of resolution on the distance from the center of the T-junction and the practical limitation of the method. Fig. 22 shows the result of the PEC sphere with the diameter 0.05 m as the point-like target placed at  $(x,y) = (0,4)$  m in the model with the wall of the T-junction continued to the target position. Fig. 22(a) shows the model, and (b) shows the result of the image. In this case, the resolution of the method is kept for the far area from the T-junction center, and the image can capture the target clearly. It can be understood that the fields on the plane  $z=0$  m in the area between the walls are held for as long as the wall continues and behaves as a superposition of propagation modes in the waveguide.

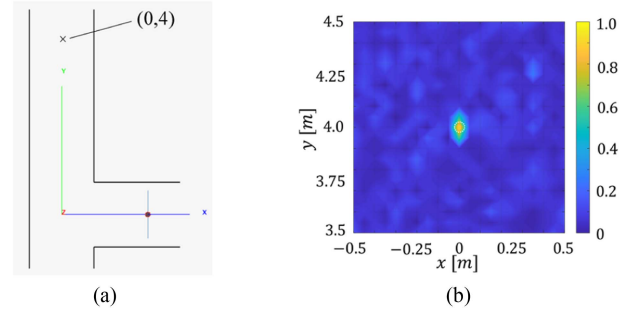


Fig. 22. Evaluation results of image resolution for the PEC sphere with diameter 0.05 m placed at  $(x,y) = (0,4)$  m in the model with the wall of the passage continued to the imaging area. (a) Top view of the model. (b) Obtained image. The singular value truncation threshold  $C$  is  $-15$  dB, the same as the main text.

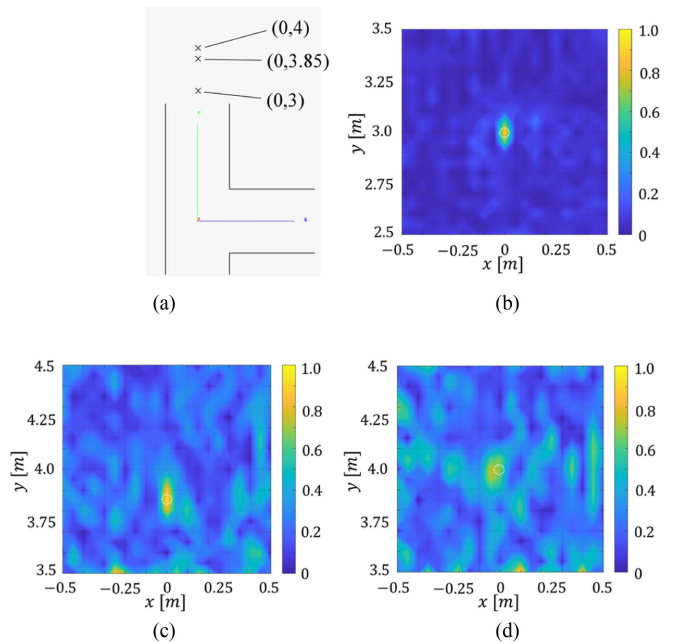


Fig. 23. Evaluation results of image resolution for the PEC sphere with diameter 0.05 m placed at  $(x,y) = (0,3)$  m,  $(0,3.85)$  m,  $(0,4)$  m in the model with the wall ended at the  $y = 2.75$  m the same as the model in the main text. (a) Top view of the model. (b) Image of the target position  $(0,3)$  m. (c) Image of the target position  $(0,3.85)$  m. (d) Image of the target position  $(0,4)$  m. The singular value truncation threshold  $C$  is  $-15$  dB, the same as the main text.

On the other hand, Fig. 23 shows the results of images for various positions of the PEC sphere with a diameter of 0.05 m in the model, with the wall ending before the imaging area. Fig. 23(a) shows the model, and (b)–(d) shows the obtained images in the results. The resolution of the images gradually degraded as they moved away from the endpoint of the passage walls, and imaging was broken down in the case  $y = 4$  m or further away area. In the area away from the endpoints of the walls, fields are no longer in waveguide mode-like distribution and tend to be in free space propagation mode. In this case, oblique incident components corresponding to the higher mode of the waveguide disappear and lead to an under-sampling situation. As a result, an aliasing ghost arises, and the method fails to obtain a localized image.

This NLOS imaging approach is limited to the target area sufficiently close to areas bounded by continuous walls, which construct the NLOS environment.

## REFERENCES

- [1] S. Li, G. Cui, S. Guo, C. Jia, L. Kong, and X. Yang, "On the electromagnetic diffraction propagation model and applications," *IEEE J. Sel. Topics Appl. Earth Observ. Remote Sens.*, vol. 13, pp. 884–895, 2020, doi: [10.1109/JSTARS.2020.2974529](https://doi.org/10.1109/JSTARS.2020.2974529).
- [2] J. He, S. Terashima, H. Yamada, and S. Kidera, "Diffraction signal-based Human recognition in non-line-of-sight (NLOS) situation for millimeter wave radar," *IEEE J. Sel. Topics Appl. Earth Observ. Remote Sens.*, vol. 14, pp. 4370–4380, 2021.
- [3] G. Gennarelli and F. Soldovieri, "Multipath ghosts in radar imaging: Physical insight and mitigation strategies," *IEEE J. Sel. Topics Appl. Earth Observ. Remote Sens.*, vol. 8, no. 3, pp. 1078–1086, Mar. 2015, doi: [10.1109/JSTARS.2014.2363233](https://doi.org/10.1109/JSTARS.2014.2363233).
- [4] S. Guo, Q. Zhao, G. Cui, S. Li, L. Kong, and X. Yang, "Behind corner targets location using small aperture millimeter wave radar in NLOS urban environment," *IEEE J. Sel. Topics Appl. Earth Observ. Remote Sens.*, vol. 13, pp. 460–470, 2020, doi: [10.1109/JSTARS.2020.2963924](https://doi.org/10.1109/JSTARS.2020.2963924).
- [5] S. Li et al., "Multiple targets localization behind L-shaped corner via UWB radar," *IEEE Trans. Veh. Technol.*, vol. 70, no. 4, pp. 3087–3100, Apr. 2021, doi: [10.1109/TVT.2021.3068266](https://doi.org/10.1109/TVT.2021.3068266).
- [6] Q. Tang, J. Li, L. Wang, Y. Jia, and G. Cui, "Multipath imaging for NLOS targets behind an L-shaped corner with single-channel UWB radar," *IEEE Sensors J.*, vol. 22, no. 2, pp. 1531–1540, Jan. 2022, doi: [10.1109/JSEN.2021.3131665](https://doi.org/10.1109/JSEN.2021.3131665).
- [7] P. Wu, J. Chen, S. Guo, G. Cui, L. Kong, and X. Yang, "NLOS positioning for building layout and target based on association and hypothesis method," *IEEE Trans. Geosci. Remote Sens.*, vol. 61, 2023, Art. no. 5101913, doi: [10.1109/TGRS.2023.3250831](https://doi.org/10.1109/TGRS.2023.3250831).
- [8] P. Setlur, T. Negishi, N. Devroye, and D. Erricolo, "Multipath exploitation in Non-LOS urban synthetic aperture radar," *IEEE J. Sel. Topics Signal Process.*, vol. 8, no. 1, pp. 137–152, Feb. 2014, doi: [10.1109/JSTSP.2013.2287185](https://doi.org/10.1109/JSTSP.2013.2287185).
- [9] S. Guo, G. Cui, L. Kong, Y. Song, and X. Yang, "Multipath analysis and exploitation for MIMO through-the-wall imaging radar," *IEEE J. Sel. Topics Appl. Earth Observ. Remote Sens.*, vol. 11, no. 10, pp. 3721–3731, Oct. 2018, doi: [10.1109/JSTARS.2018.2865746](https://doi.org/10.1109/JSTARS.2018.2865746).
- [10] S. Yue, H. He, P. Cao, K. Zha, M. Koizumi, and D. Katabi, "CornerRadar: RF-based indoor localization around corners," *Proc. ACM Interact. Mob. Wearable Ubiquitous Technol.*, vol. 6, no. 1, Mar. 2022, Art. no. 34, doi: [10.1145/3517226](https://doi.org/10.1145/3517226).
- [11] S. Fujita, T. Sakamoto, and T. Sato, "An accurate UWB radar imaging method using indoor multipath echoes for targets in shadow regions," in *Proc. Int. Conf. Indoor Positioning Indoor Navigat.*, 2010, pp. 1–7, doi: [10.1109/IPIN.2010.5647961](https://doi.org/10.1109/IPIN.2010.5647961).
- [12] S. Kidera, T. Sakamoto, and T. Sato, "Extended imaging algorithm based on aperture synthesis with double-scattered waves for UWB radars," *IEEE Trans. Geosci. Remote Sens.*, vol. 49, no. 12, pp. 5128–5139, Dec. 2011.
- [13] L. Thirion-Lefevre and R. Guinvarc'h, "Investigating the use of low frequencies in urban areas: Application to NLOS configurations," *IEEE J. Sel. Topics Appl. Earth Observ. Remote Sens.*, vol. 8, no. 7, pp. 3720–3729, Jul. 2015, doi: [10.1109/JSTARS.2015.2441293](https://doi.org/10.1109/JSTARS.2015.2441293).
- [14] J. Wei, S. Wei, X. Liu, M. Wang, J. Shi, and X. Zhang, "Non-line-of-sight imaging by millimeter wave radar," in *Proc. IEEE Int. Geosci. Remote Sens. Symp.*, 2021, pp. 2983–2986, doi: [10.1109/IGARSS47720.2021.9553059](https://doi.org/10.1109/IGARSS47720.2021.9553059).
- [15] S. Wei et al., "Nonline-of-sight 3-D imaging using millimeter-wave radar," *IEEE Trans. Geosci. Remote Sens.*, vol. 60, 2022, Art. no. 5106518, doi: [10.1109/TGRS.2021.3112579](https://doi.org/10.1109/TGRS.2021.3112579).
- [16] M. Leigsnering, M. Amin, F. Ahmad, and A. M. Zoubir, "Multipath exploitation and suppression for SAR imaging of building interiors: An overview of recent advances," *IEEE Signal Process. Mag.*, vol. 31, no. 4, pp. 110–119, Jul. 2014.
- [17] A. Brancaccio, C. Di Dio, and G. Leone, "Linear inversion of PEC scatterers," in *Proc. IEEE Int. Geosci. Remote Sens. Symp.*, 2008, pp. III–194–III–197.
- [18] R. Solimene, A. Buonanno, F. Soldovieri, and R. Pierri, "Physical optics imaging of 3-D PEC objects: Vector and multipolarized approaches," *IEEE Trans. Geosci. Remote Sens.*, vol. 91, no. 6, Aug. 2007, Art. no. 061103.
- [19] R. Solimene, A. Buonanno, F. Soldovieri, and R. Pierri, "3D shape reconstruction of PEC scatterers by PO vectorial formulation," in *Proc. Int. Conf. Electromagnetics Adv. Appl.*, 2009, pp. 592–595.
- [20] R. Solimene, F. Soldovieri, G. Prisco, and R. Pierri, "Three-dimensional through-wall imaging under ambiguous wall parameters," *IEEE Trans. Geosci. Remote Sens.*, vol. 47, no. 5, pp. 1310–1317, May 2009.
- [21] G. Gennarelli, R. Solimene, F. Soldovieri, and M. G. Amin, "Three-dimensional through-wall sensing of moving targets using passive multi-static radars," *IEEE J. Sel. Topics Appl. Earth Observ. Remote Sens.*, vol. 9, no. 1, pp. 141–148, Jan. 2016, doi: [10.1109/JSTARS.2015.2443078](https://doi.org/10.1109/JSTARS.2015.2443078).
- [22] G. Gennarelli and F. Soldovieri, "A linear inverse scattering algorithm for radar imaging in multipath environments," *IEEE Geosci. Remote Sens. Lett.*, vol. 10, no. 5, pp. 1085–1089, Sep. 2013.
- [23] R. Solimene, I. Catapano, G. Gennarelli, A. Cuccaro, A. Dell' Aversano, and F. Soldovieri, "SAR imaging algorithms and some unconventional applications: A unified mathematical overview," *IEEE Signal Process. Mag.*, vol. 31, no. 4, pp. 90–98, Jul. 2014, doi: [10.1109/MSP.2014.2311271](https://doi.org/10.1109/MSP.2014.2311271).
- [24] R. J. Burkholder, "Electromagnetic models for exploiting multi-path propagation in through-wall radar imaging," in *Proc. Int. Conf. Electromagnetics Adv. Appl.*, 2009, pp. 572–575, doi: [10.1109/ICEAA.2009.5297365](https://doi.org/10.1109/ICEAA.2009.5297365).
- [25] G. Gennarelli, G. Riccio, R. Solimene, and F. Soldovieri, "Radar imaging through a building corner," *IEEE Trans. Geosci. Remote Sens.*, vol. 52, no. 10, pp. 6750–6761, Oct. 2014, doi: [10.1109/TGRS.2014.2301882](https://doi.org/10.1109/TGRS.2014.2301882).
- [26] G. Gennarelli and F. Soldovieri, "Radar imaging through cinderblock walls: Achievable performance by a model-corrected linear inverse scattering approach," *IEEE Trans. Geosci. Remote Sens.*, vol. 52, no. 10, pp. 6738–6749, Oct. 2014, doi: [10.1109/TGRS.2014.2301851](https://doi.org/10.1109/TGRS.2014.2301851).
- [27] V. Khorashadi-Zadeh and M. Dehmollaian, "Through a cinder block wall refocusing using SAR back projection method," *IEEE Trans. Antennas Propag.*, vol. 67, no. 2, pp. 1212–1222, Feb. 2019, doi: [10.1109/TAP.2018.2882599](https://doi.org/10.1109/TAP.2018.2882599).
- [28] N. P. B. Kammersgaard, S. H. Kvist, J. Thaysen, and K. B. Jakobsen, "Validity of PEC approximation for on-body propagation," in *Proc. 10th Eur. Conf. Antennas Propag.*, 2016, pp. 1–4, doi: [10.1109/Eu-CAP.2016.7481299](https://doi.org/10.1109/Eu-CAP.2016.7481299).
- [29] Z. A. Awan and D. Seetharamdo, "Enhancement of backscattering cross section from an equivalent human cylinder under oblique incidence," *IET Microw., Antennas Propag.*, vol. 16, no. 8, pp. 497–509, 2022.
- [30] A. F. Peterson, S. L. Ray, and R. Mittra, *Computational Methods for Electromagnetics*. New York, NY, USA: IEEE Press, 1998.
- [31] R. Solimene, F. Soldovieri, G. Prisco, and R. Pierri, "Three-dimensional microwave tomography by a 2-D slice-based reconstruction algorithm," *IEEE Geosci. Remote Sens. Lett.*, vol. 4, no. 4, pp. 556–560, Oct. 2007, doi: [10.1109/LGRS.2007.900741](https://doi.org/10.1109/LGRS.2007.900741).
- [32] J. Song, C. C. Lu, and W. C. Chew, "Multilevel fast multipole algorithm for electromagnetic scattering by large complex objects," *IEEE Trans. Antennas Propag.*, vol. 45, no. 10, pp. 1488–1493, Oct. 1997.
- [33] R. Solimene, F. Ahmad, and F. Soldovieri, "A novel CS-TSVD strategy to perform data reduction in linear inverse scattering problems," *IEEE Geosci. Remote Sens. Lett.*, vol. 9, no. 5, pp. 881–885, Sep. 2012, doi: [10.1109/LGRS.2012.2185679](https://doi.org/10.1109/LGRS.2012.2185679).
- [34] X. Dong and Y. Zhang, "A novel compressive sensing algorithm for SAR imaging," *IEEE J. Sel. Topics Appl. Earth Observ. Remote Sens.*, vol. 7, no. 2, pp. 708–720, Feb. 2014, doi: [10.1109/JSTARS.2013.2291578](https://doi.org/10.1109/JSTARS.2013.2291578).
- [35] Q. Guo, X. Liang, and Y. Li, "A novel method for 3-D building structure determination in through-the-wall radar," *IEEE J. Sel. Topics Appl. Earth Observ. Remote Sens.*, vol. 17, pp. 7592–7607, 2024, doi: [10.1109/JSTARS.2024.3379213](https://doi.org/10.1109/JSTARS.2024.3379213).



**Hiroshi Suenobu** (Member, IEEE) received the B.S. degree from Kochi University, Kochi, Japan, in 2011, and the M.S. and Ph.D. degrees in physics from Nagoya University, Nagoya, Japan, in 2013 and 2017, respectively.

He joined Mitsubishi Electric Corporation, Tokyo, Japan, in 2016. He has been engaged in research on the electromagnetic field and radar cross section analysis. He is currently a Head Researcher with the Antenna Technology Department of the Information Technology Research and Development Center, Mitsubishi Electric Corporation.



**Shouhei Kidera** (Senior Member, IEEE) received the B.E. degree in electrical and electronic engineering, M.I., and Ph.D. degrees in informatics from Kyoto University, Kyoto, Japan, in 2003, 2005, and 2007, respectively.

In 2009, he joined as an Assistant Professor with the University of Electro-Communications, Tokyo, Japan, where he is currently a full Professor with Graduate School of Informatics and Engineering, University of Electro-Communications, Tokyo, Japan. He was with the Cross-Disciplinary Electromagnetics Laboratory, University of Wisconsin Madison as the visiting researcher in 2016. He was a Principal Investigator of the PRESTO Program of Japan Science and Technology Agency from 2017 to 2021. His current research interests include advanced radar signal processing, electromagnetic inverse scattering issue for ultra wideband three-dimensional sensor, bio-medical applications.

Dr. Kidera was the recipient of the 2012 Ando Incentive Prize for the Study of Electronics, 2013 Young Scientist's Prize by the Japanese Minister of Education, Culture, Sports, Science and Technology, 2014 Funai Achievement Award, 2022 KDDI Foundation Award, Contribution Award, and 2023 RIEC Award. He is a senior member of the Institute of Electronics, Information, and Communication Engineers of Japan, and the International Union of Radio Science (Union Radio-Scientifique Internationale), and a member of the Institute of Electrical Engineering of Japan, and the Japan Society of Applied Physics.

**Takayuki Nakanishi** (Member, IEEE) received the B.E. and M.E. degrees in engineering from Kyushu University, Fukuoka, Japan, in 2006 and 2008, respectively.

In 2008, he joined Mitsubishi Electric Corporation, Kamakura, Japan. He is currently a Head Researcher with the Antenna Technology Department, Information Technology Research and Development Center, Kamakura. His research interests include radio propagation, array antennas, and radar systems.

**Ryosuke Kobayashi** received the B.E. and M.E. degrees in engineering from Kanazawa Institute of Technology, Nonoichi, Japan, in 2008 and 2010, respectively.

In 2010, he joined Mitsubishi Electric Engineering Corporation, Tokyo, Japan. He has been engaged in the design and development of antennas for satellite communications and mobile communications. Currently, he is involved in the design and development of compact antennas.



**Yasuhiro Nishioka** (Member, IEEE) received the B.E., M.E., and D.E. degrees in engineering from Tokyo University of Agriculture and Technology, Tokyo, Japan, in 1995, 1997, and 2000, respectively.

In 2000, he joined Mitsubishi Electric Corporation, Tokyo. Since then, he has been engaged in research on small antennas and electromagnetic field analysis. He is currently a Manager with the Antenna Technology Department of the Information Technology Research and Development Center, Mitsubishi Electric Corporation.

Dr. Nishioka is the recipient of the Young Researcher's Award of IEICE Japan in 1998 and the IEEE Antennas and Propagation Society Tokyo Chapter Young Engineer Award in 1999. He is a regular member of the IEICE of Japan.



**Yoshio Inasawa** (Senior Member, IEEE) the B.E., M.E., and D.E. degrees in engineering from Tokyo Institute of Technology, Tokyo, Japan, in 1991, 1993, and 2008, respectively.

In 1993, he joined Mitsubishi Electric Corporation, Tokyo, Japan. Since then, he has been engaged in research on electromagnetic field analysis, radiowave propagation, reflector antennas, and satellite communication systems. He is currently a General Manager with the Antenna Technology Department of the Information Technology Research and Development Center at Mitsubishi Electric Corporation.

Dr. Inasawa is the recipient of the R&D 100 Awards in 2005.